Journal of
Materials Chemistry A

ROYAL SOCIETY
OF CHEMISTRY

COMMUNICATION

View Article Online
View Journal | View Issue

Check for updates

Cite this: *J. Mater. Chem. A*, 2025, **13**, 34220

Received 8th August 2025
Accepted 15th September 2025

DOI: 10.1039/d5ta06438d

rsc.li/materials-a

Synergy of metal halide doping and a polymeric interface enables improved electrochemical performance of all solid-state Li batteries

Madan Bahadur Saud,[a] M. Bilal Faheem,[a] Hansheng Li,[a] Haining Zhang,[a] Bilawal Khan,[b] Samprash Risal,[c] Abiral Baniya,[a] Xinlu Wang,[d] Yuchen Zhang,[a] Ruosi Qiao,[a] Poojan Kaswekar,[a] Ian Dean Hosein,[d] Yeqing Wang,[a] Jr-Hau He,[b] Zheng Fan[c] and Quinn Qiao*[a]

Sulfide solid-state electrolytes are promising candidates for all-solid-state lithium metal batteries (ASSLBs) having higher energy density and practical safety due to their high ionic conductivity and favorable mechanical properties. However, their practical integration is hindered by low critical current density (CCD), a narrow electrochemical stability window, and high impedance with electrodes. Herein, we demonstrate that doping lithium phosphorus sulfide ($Li_7P_3S_{11}$) solid electrolyte with zirconium chloride ($ZrCl_4$) significantly enhances its electrochemical performance. Unlike previously reported doping strategies, $ZrCl_4$ doping uniquely introduces dual dopants (Zr^{4+} and Cl^-) into the $Li_7P_3S_{11}$ matrix. Density functional theory (DFT) and *ab initio* molecular dynamics (AIMD) simulations reveal that the Zr^{4+} ions increase dynamic structural flexibility, while Cl^- ions create additional Li^+ vacancies, collectively enhancing structural stability and ionic conductivity beyond the capacity of single-element doping strategies. Optimized doping content of $ZrCl_4$ improved the CCD of $Li_7P_3S_{11}$ from 0.55 mA cm^{-2} to 1.7 mA cm^{-2}, while the ionic conductivity improved from 1.8×10^{-3} S cm^{-1} to 3.0×10^{-3} S cm^{-1}. Li/Li symmetrical cells with doped electrolyte exhibited improved cycling stability at 0.1 mA cm^{-2} compared to the control counterparts. Furthermore, a thin solid polymer electrolyte (SPE) was used at the interface between the cathode and solid electrolyte to enable the stack pressure free operation of full cells. Li/$LiFePO_4$ (LFP) full cells using doped solid electrolyte (SE) in combination with SPE catholyte demonstrated stable performance compared to undoped SE based cells. The enhanced Li-dendrite suppression and improved electrochemical properties due to doped $Li_7P_3S_{11}$ and the stack free operation due to the addition of SPE as catholyte will add significant potential for advancing ASSLB technology.

1 Introduction

Li-ion battery technology faces significant limitations in meeting the growing demands for higher energy density batteries, primarily due to the reliance on graphite anodes, which offer a theoretical capacity of only 372 mAh g^{-1}.[1,2] Additionally, liquid electrolytes used in them are flammable and can ignite if Li dendrites penetrate the separator and come in contact with the cathode creating a short circuit causing thermal runaway.[3] This situation underscores the urgent need for the development of safer and efficient alternatives. Replacing graphite with lithium metal to increase the energy density of current Li-ion batteries poses safety concerns, and leads to low-rate capabilities and poor cycling performance due to the formation of an unstable solid electrolyte interphase (SEI), undesired Li dendrite growth and dead Li.[2,4–7] ASSLBs, which use Li metal anodes and solid electrolytes like polymers, oxides, sulfides, and halides have emerged as a promising solution, potentially addressing both energy density limitations and safety concerns.[8–10] By eliminating the risks associated with liquid electrolytes and enabling higher capacity Li metal anodes which have high theoretical capacity (3862 mAh g^{-1} *vs.* 372 mAh g^{-1} for graphite) and low redox potential (−3.04 V), ASSLBs have shown great potential in battery technology, paving the way for next-generation energy storage applications.[8,11,12]

ASSLBs have the potential to enhance energy densities from the current ∼270 Wh kg^{-1} to above 500 Wh kg^{-1} while suppressing the safety issues associated with conventional Li-ion batteries. It is essential to successfully pair solid electrolytes with Li metal anodes and high-capacity transition metal oxides, sulfur, and oxygen cathodes.[8,13–15] Various types of solid Li-ion conductors including solid polymers, oxides, halides and sulfides, have been reported and implemented as solid electrolytes.[9,16–19] While SPEs offer excellent mechanical flexibility and ease of fabrication, their performance in ASSLBs is often limited by low ionic conductivity at ambient temperatures, minimal CCD, and instability with Li metal anodes. Oxide electrolytes, like Li lanthanum zirconate (LLZO) and Li titanium

---

[a] *Energy Conversion and Storage Lab, Mechanical and Aerospace Engineering, Syracuse University, Syracuse, NY 13244, USA. E-mail: quqiao@syr.edu*

[b] *Department of Materials Science and Engineering, City University of Hong Kong, Kowloon, 999077, Hong Kong*

[c] *Materials Science and Engineering Program and Texas Center for Superconductivity at the University of Houston, University of Houston, 4726 Calhoun Rd, Houston, Texas 77204, USA*

[d] *Department of Biomedical and Chemical Engineering, Syracuse University, Syracuse, NY 13244, USA*

oxide (LTO), often require high processing temperatures, exhibit brittleness and suffer from poor contact with Li metal, which challenge their practical applications in solid-state batteries.[17] Sulfide electrolytes including $Li_7P_3S_{11}$, Li_6PS_5Cl, and $Li_{10}GeP_2S_{12}$ exhibit significantly higher ionic conductivities than their oxide counterparts due to the weaker Li–S interactions, which facilitate faster Li-ion transport, making them promising candidates for ASSLBs.[20–24] Furthermore, sulfide electrolytes can be synthesized at lower temperatures compared to oxides and can be cold pressed, while reducing the energy consumption.[20] $Li_7P_3S_{11}$, a superionic conductor first reported by Mizuno *et al.*,[21] stands out as one of the most promising sulfide electrolytes for the development of high-energy-density ASSLBs. $Li_7P_3S_{11}$ crystallizes in a triclinic cell, space group $P\bar{1}$ (SI Fig. S1A) and reveals a quick and extremely complex translational movement of Li-ions along zigzag chains in the open space between $P_2S_7{}^{4-}$ di-tetrahedra and slightly distorted $PS_4{}^{3-}$ tetrahedra.[25,26] Room temperature ionic conductivities ranging from 10^{-4} S cm^{-1} to 10^{-2} S cm^{-1} have been reported for this electrolyte depending on the synthesis routes.[27–30] However, its integration into ASSLBs is impeded by several factors, including low CCD, a narrow intrinsic electrochemical stability window, and poor chemical compatibility with electrodes.[20,31] The reported room temperature CCDs for $Li_7P_3S_{11}$ are typically less than 1 mA cm^{-2}, which is insufficient for effective practical applications such as fast charging of Electric Vehicles (EVs).[32,33] Doping $Li_7P_3S_{11}$ electrolyte with various impurity elements has been investigated as a potential strategy to enhance CCD and ionic conductivity. Doping can alter the structural and electrochemical properties of SEs, facilitating improved performance. Several doping agents, including MoS_2, In_2S_3, ZrO_2, ZnO, CaI_2, Ce_2S_3, $SnSe_2$, AgCl, *etc.* have been studied; however, their impact on increasing CCD of $Li_7P_3S_{11}$ has generally been modest.[28,32,34–38]

In this work, we introduced a novel dopant $ZrCl_4$ to $Li_7P_3S_{11}$, that led to a significant enhancement in its CCD and ionic conductivity. The introduction of a minute amount of $ZrCl_4$ through the synthesis process sustained the crystal structure of $Li_7P_3S_{11}$, while the CCD increased markedly from 0.55 mA cm^{-2} to 1.7 mA cm^{-2} at room temperature. In addition to CCD improvements, optimized doping concentration increased the ionic conductivity from 1.8×10^{-3} S cm^{-1} to 3.0×10^{-3} S cm^{-1} and lowered the activation energy from 0.26 eV to 0.23 eV. Furthermore, the interface stability with a Li metal anode was enhanced as Li/Li symmetrical cells with control SE cycled only for 110 h whereas cells with engineered solid electrolyte (ESE) cycled for more than 500 h at 0.1 mA cm^{-2}. More importantly, incorporation of SPE catholyte enabled full cells with device architecture Li/SE/SPE/LFP to cycle well without applying any stack pressure and without any protective coating on LFP cathode particles. Full cells with ESE demonstrated higher specific capacity and stable performance compared to the control SE for 50 cycles at 0.1C. Additionally, the DFT and AIMD based simulations were conducted to investigate the structural variations of $Li_7P_3S_{11}$ due to doping, emphasizing the role of dual dopants in altering the structure while improving the ionic conductivity.

2 Results and discussion

2.1. Structural characterization

We synthesized solid electrolytes using the solid state route that involves planetary ball milling of precursors followed by heat treatment. High-speed ball milling breaks the parent chemical bonds of the raw materials Li_2S and P_2S_5 promoting the atomic-level homogenous mixing. Different ball milling durations have been reported in the literature for the synthesis of crystalline $Li_7P_3S_{11}$.[39–41] The ball milling duration for the complete reaction between the Li_2S and P_2S_5 precursors is influenced by the amount/quality of the precursors, size, number of balls, and size/type of milling jars used.[41] We optimized the ball milling duration for the complete reaction between the precursors taking 494 mg of precursors and 10 stainless steel (SS) balls of diameter 8 mm in each 100 ml SS jar. SI Fig. S2 shows the X-ray diffraction (XRD) spectrum of the Li_2S precursor and ball-milled $Li_7P_3S_{11}$ after 8 h and 16 h of ball milling. The 8 h ball-milled samples show prominent Li_2S peaks, indicating that the solid-state reaction between the precursors has not yet completed. However, the XRD spectrum of the 16 h ball-milled sample shows no detectable peaks, indicating that the precursors have fully reacted to form an amorphous $Li_7P_3S_{11}$ phase.

Following ball milling, the samples were heat-treated to convert the amorphous $Li_7P_3S_{11}$ into crystalline $Li_7P_3S_{11}$. Since the ionic conductivity depends on the degree of crystallinity and purity of the sample, optimal heat treatment temperature and time are crucial. Various heat treatment conditions, *i.e.* temperature (200–300 °C) and time (1–5 h) have been reported in the literature, resulting in different values of ionic conductivity.[42–44] To find the optimal heat treatment duration for phase pure crystalline $Li_7P_3S_{11}$, the ball-milled amorphous precursor was heat treated at 240 °C for 0.5 h, 1 h, and 2 h inside an argon filled glovebox. SI Fig. S3 shows the XRD patterns of heat-treated samples. Sharp peaks that align with the PDF standard card (ICSD: 157654) corresponding to crystalline $Li_7P_3S_{11}$ are present in all the samples.[25] However, the XRD peaks of the 0.5 h-treated sample are broader than those of the samples with 1 h and 2 h heat treatment duration. This is attributed to the presence of an amorphous phase in a 0.5 h heat treated sample. There is no discernible difference in the XRD patterns between 1 h and 2 h heat treated samples. This shows that 1 h heat treatment is sufficient to achieve the desired crystallinity. So, the next batches of synthesis were performed using 1 h heat treatment at 240 °C.

After optimizing the heat treatment duration and temperature, $Li_7P_3S_{11}$ SEs with 1, 2, 3, and 4 wt% doping contents (denoted as ESE-1, ESE-2, ESE-3, and ESE-4 hereafter) were synthesized. Fig. 1A shows the XRD patterns of control SE and ESE with various wt% contents. All samples show sharp diffraction peaks corresponding to crystalline $Li_7P_3S_{11}$ and no additional peaks are observed in the XRD pattern of ESE. The absence of any significant additional peaks in the XRD pattern of ESE indicates that no new crystalline phases are formed upon doping with a small amount of $ZrCl_4$ which is consistent with previous reports on doped $Li_7P_3S_{11}$.[25,32,45,46] However, subtle

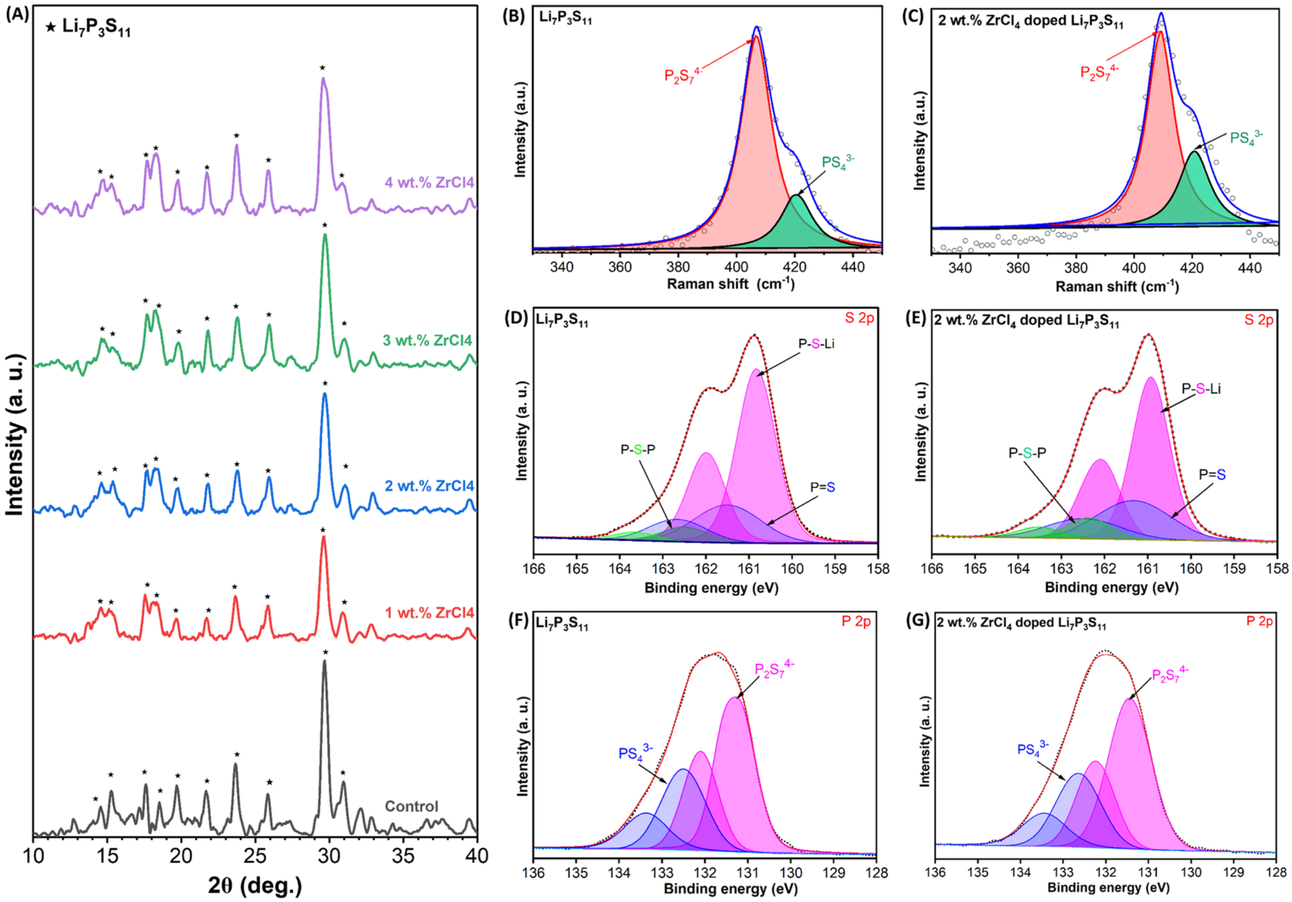

Fig. 1 (A) XRD spectra of control SE and ESE (B and C); Raman spectra of control SE and ESE-2; (D–G) XPS detail spectra of the control SE and ESE-2 for the S 2p and P 2p signals.

changes such as lattice parameter variations or local distortions may still occur, as expected from the introduction of Zr^{4+} and Cl^- ions.

Furthermore, to better understand the structural effects of $ZrCl_4$ doping on $Li_7P_3S_{11}$, Rietveld refinement was carried out on the XRD data, and the detailed results are provided in supplementary Fig. S4 and Table S2. The Rietveld refinement of ESE-2 showed a good fit into the $Li_7P_3S_{11}$ crystal structure, with a low R_{wp} value (≤ 2.051) suggesting that most Zr and Cl atoms are successfully incorporated into the $Li_7P_3S_{11}$ solid electrolyte matrix. Importantly, no new unidentified peaks were observed, and the background was well-fitted, pointing to a largely crystalline structure with minimal amorphous content. A few minor reflections can be attributed to $ZrCl_4$, which may suggest the presence of a residual dopant or a small amount of the secondary phase. Overall, these results suggest that $ZrCl_4$ doping does not disrupt the fundamental crystal structure of $Li_7P_3S_{11}$ but may introduce subtle modifications without forming significant impurity phases.[47] As shown in SI Fig. S4F, the peak shift with the doping of $ZrCl_4$ is observed towards lower angles, which according to Bragg's law is due to the increase in lattice parameters. This finding is further confirmed by the increase in unit cell volume (V) as revealed through Rietveld refinement (SI Fig. S4). As shown in SI Table S2, the Rietveld refinement results reveal a slight increase in the lattice parameters of $Li_7P_3S_{11}$ after doping. These observations suggest that the Zr and Cl atoms are incorporated into the $Li_7P_3S_{11}$ crystal structure.

Raman spectra of control SE and ESE-2 were obtained to reveal the local structure of P–S polyhedra before and after doping. The wide range spectrum is shown in SI Fig. S5 The Raman spectra between the wavenumbers 330 to 450 cm^{-1} of control SE and ESE shown in Fig. 1(B and C) exhibit peaks corresponding to the stretching vibration of P–S bonds in the PS_4^{3-} (*ortho*-thiophosphate tetrahedra) and $P_2S_7^{4-}$ (*pyro*-thiophosphate ditetrahedra) ions which are the characteristic Raman peaks of $Li_7P_3S_{11}$.[46,48] The PS_4^{3-} peak appears at 420.87 cm^{-1} for both control SE and ESE whereas the $P_2S_7^{4-}$ peak shifts to an upper wavenumber from 406.81 cm^{-1} for control sample SE and to 409.61 cm^{-1} for ESE. The upward shift in the Raman peak corresponding to $P_2S_7^{4-}$ after doping confirms that the $ZrCl_4$ doping affects the P–S bonds and the inherent structure is not altered.[48] Specifically, the incorporation of Zr^{4+} and Cl^- influences local bond strengths and lattice vibrations due to the difference in their electronegativities compared with that of P and S leading to a stiffer lattice structure and altered vibrational frequencies of the P–S bonds within the $P_2S_7^{4-}$ units.[48–50] Furthermore, an additional peak appeared at 495.51 cm^{-1} (SI Fig. S5) in ESE-2 which is due to the formation of new Zr–S bonds creating novel Li^+ ion channels.

X-ray photoelectron spectroscopy (XPS) measurements were performed for the control SE and ESE-2 powder to determine the types and bonding environment of the elements present in them. The wide-scan XPS survey spectrum is shown in SI Fig. S6A. The survey spectrum of control SE exhibited the dominant peaks of P, S, C, and O, while that of ESE showed two additional peaks associated with Zr and Cl, confirming the presence of dopant elements. The presence of the C 1s and O 1s peak is due to the presence of hydrocarbon species as surface contamination which might have occurred during the sample preparation for XPS.[51] As shown in SI Fig. S1B, the PS_4^{3-} and $P_2S_7^{4-}$ units in the crystal structure of $Li_7P_3S_{11}$ contain one bridging (P–S–P), three double bond (P═S), and seven P–S–Li sulfur atoms in total.[52] These sulfur species have different binding energies. High-resolution S 2p and P 2p XPS spectra that were obtained by taking scans with an energy step size of 0.1 eV of electrolyte powders are shown in Fig. 1D–G. The S 2p spectrum clearly shows two distinct peaks, namely S $2p_{3/2}$ and S $2p_{1/2}$ due to spin–orbit coupling. To assign the peaks to three different species of sulfur, the obtained S 2p spectra were deconvoluted by using the XPS peak fitting software. The S $2p_{3/2}$ peaks corresponding to the P–S–Li, P═S, and P–S–P vibrations were found at the peak positions 160.8 eV, 161.4 eV, and 162.4 eV respectively for control SE. These values are in close agreements with the earlier reports.[33,52] For ESE these peaks are obtained at 160.93 eV, 161.32 eV, and 162.36 eV, respectively. The difference in the binding energy values after doping shows the change in the bonding environment within the sample. Similarly, the P 2p spectrum shows two distinct peaks corresponding to *ortho*-thiophosphate (PS_4^{3-}) and *pyro*-thiophosphate ($P_2S_7^{4-}$) species at 132.5 eV and 131.3 eV respectively for both control and doped samples. Due to the spin–orbit coupling effect these species can be deconvoluted into two spin–orbit components. The binding energies for Zr $3d_{5/2}$ and Zr $3d_{3/2}$ spin–orbit split components are observed at 181.12 eV and 183.29 eV respectively (SI Fig. S6B). Similarly, the binding energies for Cl $2p_{3/2}$ and Cl $2p_{1/2}$ spin–orbit split components are observed at 197.94 eV and 199.63 eV respectively (SI Fig. S6C).

The microstructures of the control SE and ESE-2 powders were analyzed using Scanning Electron Microscopy (SEM), and the results are shown in Fig. 2A and B. Both samples show the pseudo-spherical shapes attributed to primary particles of less than 2 μm size, and each particle is aggregated and connected with the others to form larger secondary particles. The control sample (Fig. 2A) exhibits agglomerated particles with irregular shapes and rough, porous surfaces, and the particle size distribution is non-uniform, with smaller grains forming loosely packed clusters. These features indicate potential limitations in achieving uniform conducting pathways, which could hinder ionic conductivity and interface stability. In contrast, the ESE (Fig. 2B) shows more compact and fused particles with smoother surfaces and comparatively reduced porosity. These morphological improvements reduce grain boundary resistance and improve structural integrity, thereby enhancing ionic transport properties and CCD. The observed changes in particle morphology directly correlate with the improved electrochemical performance of the doped sample. EDS mappings as shown in SI Fig. S7(A and B) demonstrate the uniform distribution of P, S, and the introduced dopants, Zr and Cl, within the electrolyte particles after doping.

2.2. Electrochemical characterization

Solid electrolytes with ionic conductivity on the order $>10^{-4}$ S cm^{-1} are essential for developing a high-energy bulk-type ASSLB.[53] Room-temperature ionic conductivities in the range of 10^{-4} to 10^{-2} S cm^{-1} have been reported for $Li_7P_3S_{11}$ by different research groups.[27,29,54,55] The observed discrepancies in the ionic conductivity arise due to the difference in synthesis methods, pellet fabrication pressure, applied stack pressure during measurement, and types of blocking electrodes used. We evaluated the ionic conductivity of $Li_7P_3S_{11}$ before and after heat treatment. Ionic conductivity of $Li_7P_3S_{11}$ pellets was calculated using the formula given in eqn (1) below:

$$\sigma = \frac{L}{A \times R} \tag{1}$$

where L is the electrolyte pellet thickness, A is the contact area between blocking electrodes and the pellet, and R is the electrolyte impedance. Obtained Nyquist plots of SS/$Li_7P_3S_{11}$/SS ion blocking cells and calculated ionic conductivities are shown in Fig. 2(E and F). It is observed that the ionic conductivity increased with the increase in heat treatment temperature up to 240 °C and then decreased with a further increase. The ionic conductivity of the pellet using amorphous $Li_7P_3S_{11}$ is 0.3 mS cm^{-1} whereas that of the pellets using the 240 °C heat treated $Li_7P_3S_{11}$ is 1.8 mS cm^{-1}. This shows that the heat treatment of amorphous $Li_7P_3S_{11}$ increases ionic conductivity which is consistent with previous reports.[54,55] After heat treatment, PS_4^{3-} (*ortho*-thiophosphate) tetrahedra and $P_2S_7^{4-}$ (*pyro*-thiophosphate) ditetrahedra in amorphous $Li_7P_3S_{11}$ are arranged in a crystalline structure to form an interconnected network of tetrahedrally coordinated Li-ion sites resulting in a higher ionic conductivity.[25,55] The ionic conductivity of the resulting glass ceramic electrolytes is influenced by the crystalline phases present after the heat treatment.[56] But as the temperature is further increased to 260 °C, ionic conductivity decreased which might be due to the decomposition of $Li_7P_3S_{11}$ into less conductive impurity phases such as $Li_4P_2S_6$. After optimizing the heat treatment temperature for the highest ionic conductivity, we investigated the effects of $ZrCl_4$ doping concentration on Li^+ ionic conductivity. The Nyquist plots of SS/SS blocking cells using ESEs as solid electrolytes are shown in Fig. 2(E, F, H and I). The plots for both control SE and ESE followed a typical trend observed in sulfide superconductors, appearing largely as a straight line with no apparent semicircle, which reflects their outstanding ionic conductivity with negligible grain boundary resistance.[57] From Fig. 2 (G) we see that ionic conductivity increases with the addition of 1 and 2 wt% dopant whereas it decreased on increasing the doping percentage further to 3 and 4 wt%. The detailed calculation of ionic conductivity with the change in temperature and the doping percentage is shown in Table S4. The ionic conductivity of ESE-2 is the maximum reaching the value 3.0×10^{-3} S cm^{-1} which is 67 times higher than that of the control one. When Zr^{4+}

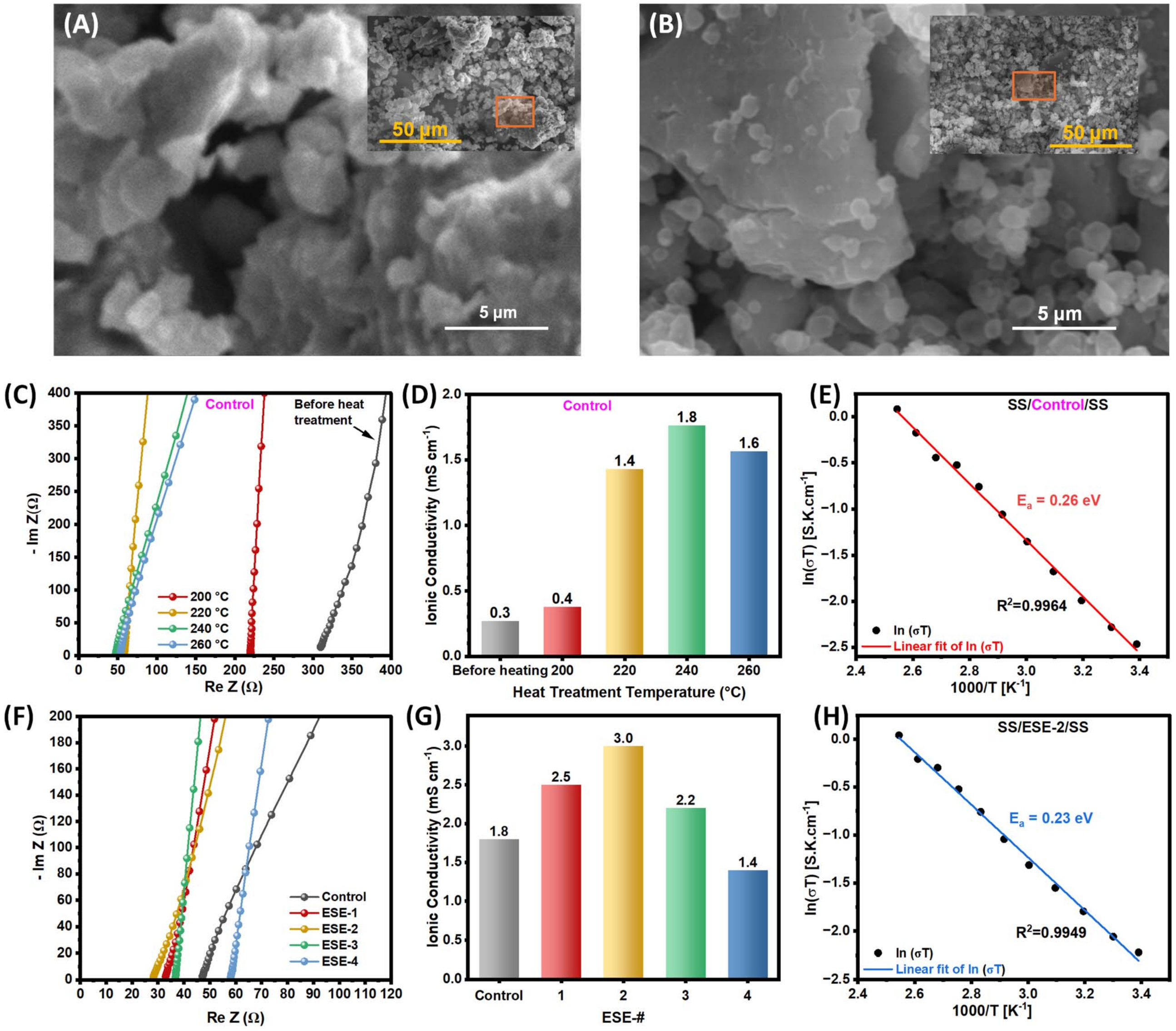

Fig. 2 SEM images of (A) $Li_7P_3S_{11}$ powder and (B) ESE-2; (C) Nyquist plots of SS/SS ion blocking cells using control SE before and after heat treatment; (D) corresponding ionic conductivity; (F) Nyquist plots of SS/SE/SS ion blocking cells using control and various wt% doped ESE; (G) corresponding ionic conductivity; (E and H) Arrhenius plots of SS/control SE/SS and SS/ESE-2/SS.

substitutes for Li^+ in the $Li_7P_3S_{11}$ structure, more Li vacancies are formed to maintain the charge neutrality. And these vacancies create pathways that enhance Li^+ mobility thereby increasing the ionic conductivity.[48] In addition, the presence of highly electronegative Cl decreases the electron cloud density on the surface of $P_2S_7{}^{4-}$ and $PS_4{}^{3-}$ units, reducing their binding to Li^+ and thus increasing the ionic conductivity.[58] However a further increase in the doping level causes an ion clogging phenomenon leading to a decrease in ionic conductivity.[33] The mechanism behind the change in ionic conductivity due to doping is further explained in Section 2.4. Due to the highest ionic conductivity of ESE-2, the rest of the tests and characterization studies were performed using the control SE and ESE-2.

Activation energy for Li^+ diffusion was evaluated by measuring the temperature dependent ionic conductivity at different temperatures ranging from 30 °C to 120 °C. Fig. 2(E and H) shows the Arrhenius plots of SS/control SE/SS and SS/ESE-2/SS cells used in the measurement, respectively. The activation energy was calculated by using the slope (σ) of the fitted line using Arrhenius eqn (2) given below[33]

$$\sigma = A\exp\left(-\frac{E_a}{KT}\right) \tag{2}$$

Here, σ, A, T and K represent the Li-ion conductivity, pre-exponential factor, absolute temperature, and Boltzmann constant, respectively. The calculated activation energy of control SE is 0.26 eV and that of ESE-2 is 0.23 eV. This suggests that $ZrCl_4$ doping can effectively reduce the activation energy and enhance the Li-ion conductivity of solid electrolyte. When $ZrCl_4$ was introduced into the $Li_7P_3S_{11}$ structure, many defects were created, and the transmission channels of Li ions are broadened simultaneously leading to a lower barrier to the transmission of Li ions and thus reducing the activation energy. Further detailed explanations are provided in Section 2.4.

Electrochemical stability of control SE and ESE-2 with Li metal was determined by conducting cycling voltammetry (CV) in the potential range from −0.5 V to 5 V (*vs.* Li/Li$^+$) at a scan rate of 1 mV s^{-1} at room temperature. SI Fig. S8(A and B) shows the CV curves of asymmetric Li/SE/SS cells using control SE and ESE, respectively. Both voltammograms show sharp oxidation and reduction peaks, corresponding to the Li stripping (oxidation Li → Li$^+$ + e$^-$) and Li plating (reduction Li$^+$ + e$^-$ → Li) occurring on the stainless-steel electrode near 0 V *vs.* Li/Li$^+$.[46] No other obvious peaks are observed in the voltage range from −0.5 to 5 V *vs.* Li/Li$^+$. This result indicates that both electrolytes exhibit a wide electrochemical window up to 5 V *vs.* Li/Li$^+$. However, the fluctuation was observed in CV curves of control SE between 4 V and 5 V indicating the slight instability between Li metal and $Li_7P_3S_{11}$ due to side reactions whereas no such fluctuation occurred in case of ESE. This shows that ESE-2 is more stable with Li metal compared to control SE at higher voltages too.

2.3. Li/Li symmetrical cells and full cell performance

Li/Li symmetrical cells were assembled in polyether ether ketone (PEEK) die cells using the control SE and ESE pellets and stripping/plating tests were conducted to evaluate the CCD. CCD, a measure of the Li dendrite suppression ability of an electrolyte, is defined as the minimum current density at which the Li dendrites penetrate the SE causing a short circuit in the cell.[48,59] On increasing the current density to a certain value, the voltage starts dropping which is an indication of dendrite penetration into the solid electrolyte.[60] In case of full penetration causing a short circuit, overpotential rapidly drops to near zero. The corresponding current density at the short circuit point is called CCD. To investigate the change in CCD of $Li_7P_3S_{11}$ due to doping, time-controlled Li plating/stripping tests were conducted on Li/Li symmetrical cells using control SE and ESE-2. The galvanostatic cycling tests were conducted with step-increased current densities at room temperature. Starting from 0.05 mA cm^{-2} the current densities were increased by 0.05 mA cm^{-2} for the initial 20 cycles and by 0.1 mA cm^{-2} after 20 cycles. Fig. 3A shows the time–voltage profile of Li/Li symmetrical cells used for CCD. Li/Li symmetrical cells with ESE-2 showed lower bulk resistance, interfacial resistance and charge transfer resistance (Fig. 3 B and SI Table S3) (Fig. 3A) than the cells with control SE which resulted in lower overpotential. Also, Li/Li symmetrical cells with control SE show a sudden drop in overpotential at a current density of 0.55 mA cm^{-2} which is an indication of Li dendrite penetration into the control SE. Therefore, the CCD of control SE is determined to be 0.55 mA cm^{-2}. However, the Li/Li symmetrical cell with ESE showed a decrease in overpotential at a significantly higher

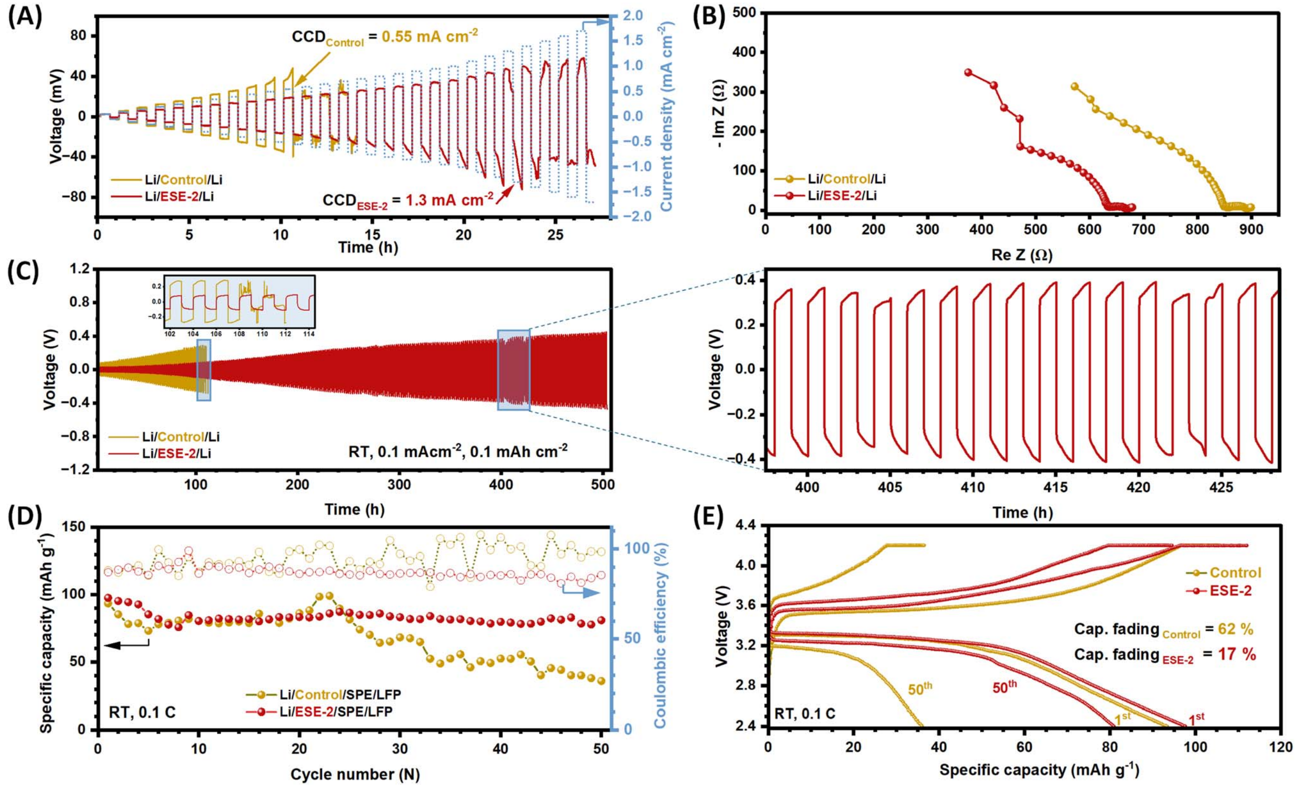

Fig. 3 (A and B) Time *vs.* voltage profile for the CCD test and impedance plots for Li/SE/Li symmetrical cells used for the CCD test; (C) cycling profile of Li/SE/Li symmetrical cells at 0.1 mA cm^{-2} with a charge discharge duration of 1 h each; (D) long-term cycling performance of Li/LFP full cells using control SE and ESE-2 at 0.1C and room temperature; (E) 1st and 50th cycle charge/discharge voltage profiles of Li/LFP full cells using control SE and ESE-2 at 0.1C and room temperature.

current density of 1.7 mA cm^{-2}. This shows that Li dendrites did not penetrate the ESE-2 up to a high current density of 1.7 mA cm^{-2}. Hence, the introduction of a small quantity of $ZrCl_4$ into the $Li_7P_3S_{11}$ structure can increase the dendrite suppression ability of $Li_7P_3S_{11}$ significantly which is beneficial for better rate capability and fast charging application of batteries. The increase in CCD is attributed to the lower charge transfer resistance, as observed in the EIS spectra shown in Fig. 3B, the increase in ionic conductivity and the possible formation of a highly insulating LiCl at the Li/SE interface due to the reaction between Li metal and ESE-2.[33,61]

Long-term cycling stability of Li metal with synthesized solid electrolytes was investigated by electrochemical cycling of Li/Li symmetrical cells in CR-2032 type coin cells at a current density of 0.1 mA cm^{-2} with a charge–discharge time of 1 h each. The results presented in Fig. 3C explain that the symmetrical cell with ESE has a lower onset overpotential compared to control SE, which is attributed to the higher ionic conductivity of ESE than the control one. It has been reported earlier that an increase in ionic conductivity due to MoS_2 doping increased the CCD of $Li_7P_3S_{11}$.[32] Both cells showed a gradual increase in overpotential with an increase in the number of cycles. This is due to the increased charge transfer resistance in the cells as seen in their impedance spectra shown in SI Fig. S9 which is due to the formation of less conductive interphases Li_2S and Li_3P at the Li/$Li_7P_3S_{11}$ interface during cycling.[52] However, the overpotential increase rate in ESE-2 is lower compared to that of control SE which proves that the ESE-2 is kinetically more stable than control SE against Li metal upon electrochemical cycling. Also, the symmetrical cells with control SE cycled only up to 110 hours before short circuiting whereas the cells with ESE-2 did not short circuit for more than 500 hours. The right panel of Fig. 3C shows the uniform stripping/plating of Li at 400–428 h of cycling at a stabilized overpotential, which further proves that the $ZrCl_4$ doping increased the long-term stability of electrolyte with Li-metal by minimizing the detrimental side reactions between Li and $Li_7P_3S_{11}$.

To evaluate the impact of doping on the electrochemical performance of ASSLBs, full cells (CR2032 coin cells) with a device architecture of Li/SE/SPE/LFP were assembled. An SPE interlayer was employed between the LPS pellet and LFP cathode to address two key challenges in current ASSLBs. Current ASSLBs are operated at a high external pressure ranging from a few MPa to several hundred MPa which is impractical for real-world use. Also, since the sulfide electrolytes are oxidized by high-voltage cathodes leading to a high interfacial resistance that degrades cycling stability, protective coatings on cathodes are required with additional cost and complexity. Here, both challenges are mitigated by using a thin layer of easily synthesized SPE which not only eliminated the need for applying stack pressure but also made cycling possible using uncoated cathodes. This cell architecture is reported with $Li_7P_3S_{11}$ for the first time, to the best of our knowledge. Galvanostatic charge/discharge measurements were conducted in the voltage range of 2.4 V to 4.2 V at 0.1C and room temperature. Specific capacity and coulombic efficiency variations of full cells up to 50 cycles are shown in Fig. 3D while the 1st and 50th capacity *vs.* voltage profiles are shown in Fig. 3E. The initial discharge capacities of the cells with control SE and ESE-2 are 93.4 mAh g^{-1} and 97.6 mAh g^{-1}, respectively. After 50 cycles, the discharge capacity of the cell using control SE decreased by 62% to 36 mAh g^{-1}, while the cell with ESE exhibited a significantly lower capacity fade of only 17% while retaining 81 mAh g^{-1}. Also, the voltage profiles shown in Fig. 3E showed small voltage polarization for cells with ESE after 50 cycles compared to the full cells with control SE. The enhanced performance is because the ESE-2 has higher ionic conductivity and forms a favorable interphase with Li metal during cycling compared to that of control SE as seen by the stable overpotential of Li/Li symmetrical cells shown in Fig. 3C. The slight variation in specific capacities during long-term cycling is attributed to fluctuations in the temperature of the battery testing room.[62] The higher initial discharge capacity and the stable cycling performance with reduced capacity fading over 50 cycles highlight the benefits of using ESE as a promising sulfide solid electrolyte.

2.4. Li^+ diffusion mechanisms

The $Li_7P_3S_{11}$ crystal unit cell comprises 14, 6, and 22 symmetrically distinct Li^+, P^{5+}, and S^{2-} sites, respectively. To ensure adequate separation between defects and dopants, a $[2 \times 1 \times 1]$ supercell containing 84 atoms was constructed (Fig. 4A). The dopant $ZrCl_4$ contributes Zr^{4+} cations and Cl^- anions. Among them, Zr^{4+} can replace four Li^+ (one Li^+ site and three Li^+ vacancies) or substitute for one P^{5+}. P^{5+} has three unique sites, labeled as P#1, P#2, and P#3 in Fig. 4A. When Cl^- replaces S^{2-}, the charge imbalance necessitates the introduction of the Li^+ vacancy. With four Cl^- available, more than 30 000 possible configurations can arise. To lower computational costs and efficiently identify preferential dopant and vacancy sites, we first calculated the electrostatic energies for all possible configurations before simulating Li diffusion. Fig. 4B illustrates the distribution of four Cl^- dopants based on 100 stable $Li_{24}P_{12}S_{40}Cl_4$ configurations with the lowest electrostatic energies. A value of *0* means all four Cl^- are inserted into PS_4^{3-} (∼1%), while 4 signifies that all four Cl^- are in $P_2S_7^{4-}$. For configurations with 2 Cl^- doped in $P_2S_7^{4-}$ (∼44%), the majority (∼74%) form two di-tetrahedral $P_2S_6Cl^{3-}$ units. Similarly, with the 3 Cl^- doped in $P_2S_7^{4-}$ (∼35%), the most common configuration involves three di-tetrahedral $P_2S_6Cl^{3-}$ units. These results indicate a preference for Cl^- to replace corner S^{2-} in $P_2S_7^{4-}$, while bridge S sites remain unoccupied, consistent with the literature.[24] Furthermore, $P_2S_6Cl^{3-}$ is more favorable for structures exhibiting low electrostatic energy compared to $P_2S_5Cl_2^{2-}$ and PS_3Cl^{2-}. Based on these findings, the structures were geometrically optimized using DFT to identify the most stable configuration. The $Li_{25}P_{11}ZrS_{40}Cl_4$ structure featuring P#1 and four $P_2S_6Cl^{3-}$ units, as depicted in Fig. 4C, was found to have the lowest total free energy. To reveal the mechanism behind the increase in ionic conductivity and improved stability with Li metal due to doping, we separately analyzed the effects of Cl^- doping and Zr^{4+} doping and their combined impact on Li^+ ionic conductivity and total energy using AIMD simulations. Fig. 4D presents the results of Cl^- doping as the number of Cl^- increases from 1 to 4. The right *y*-axis (blue) represents the free

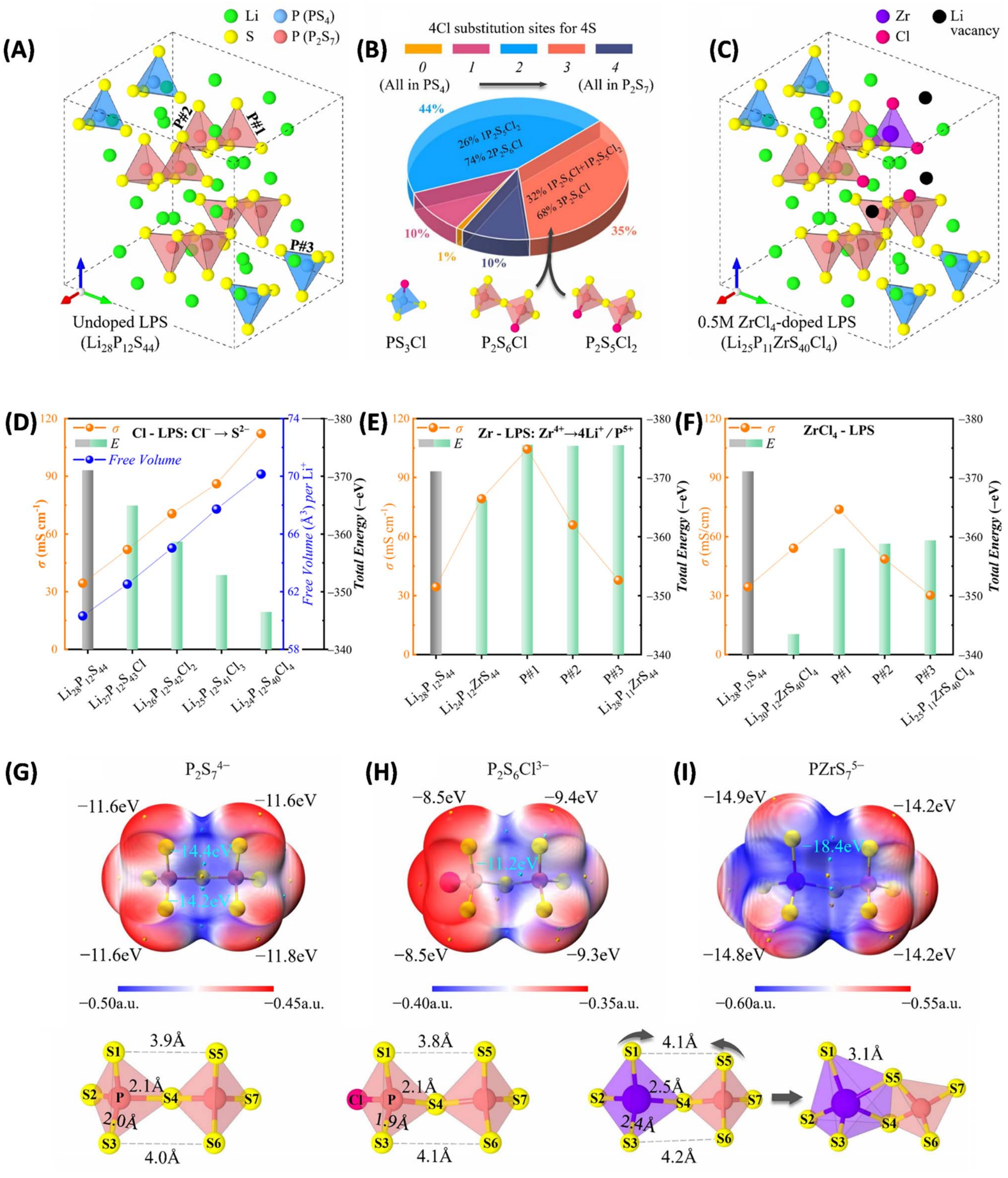

Fig. 4 (A) Crystal structure of undoped $Li_{28}P_{12}S_{44}$. (B) Ratios of Cl dopant positions (number of Cl in $P_2S_7^{4-}$) based on 100 stable $Li_{24}P_{12}S_{40}Cl_4$ configurations with the lowest electrostatic energies. (C) 0.5 M (11.4 wt%) $ZrCl_4$-doped $Li_{28}P_{12}S_{44}$ structure. Variations of the ionic conductivity and total free energy in different configurations. (D) Cl doped $Li_{28}P_{12}S_{44}$, (E) Zr doped $Li_{28}P_{12}S_{44}$ and (F) $ZrCl_4$-doped $Li_{28}P_{12}S_{44}$ electrostatic potential (ESP) and atomic spacing bond lengths of (G) $P_2S_7^{4-}$, (H) $P_2S_6Cl^{3-}$ and (I) $PZrS_7^{5-}$. The red region represents high ESP while the blue region represents a low ESP. The cyan/yellow balls represent sites with local minimum/maximum ESP values, respectively.

volume per Li^+, which is defined as the structure volume minus the tetrahedral volume ($P_2S_7^{4-}$ and PS_4^{3-}) divided by the number of Li^+. The left *y*-axis (black) depicts the total free energy of various configurations, where larger energy values correspond to more stable configurations. It is clear that the ionic conductivity increases on doping more Cl^-, aligning with the trend in the free volume per Li^+.[63] In other words, the ionic conductivity is sensitive to the Li^+ vacancy concentration. Specifically, ionic conductivity improves from 34.4 mS cm^{-1} ($Li_{28}P_{12}S_{44}$) to 112.2 mS cm^{-1} ($Li_{24}P_{12}S_{40}Cl_4$). However, with chlorine content increasing, the free energy decreases, suggesting that the structure becomes unstable. Hence the optimal concentration of the $ZrCl_4$ dopant is crucial for improving the ionic conductivity as we have observed in experimental results.

Unlike Cl^- doping, there are two cases of Zr^{4+} doping: Zr^{4+} substitution for Li^+ and Zr^{4+} substitution for P^{5+}. Case I: one Li^+ site is replaced by one doped Zr^{4+}, creating three Li^+ vacancies to maintain electronic neutrality of the structure.[64] Case II: one inserted Zr^{4+} replaces one P^{5+} with similar oxidation states. An additional Li was not introduced as its placement would be too arbitrary and artificial. Obviously, Case II exhibits a different mechanism due to the absence of Li^+ vacancies. As depicted in Fig. 4E, although Li^+ vacancies are introduced in Case I, they do not yield the highest ionic conductivity. Instead, the configuration where Zr^{4+} replaces P#1 (in $P_2S_7{}^{4-}$) achieves the maximum ionic conductivity, approximately 200% higher than that of $Li_{28}P_{12}S_{44}$. Total energy minimization indicates that P-site substitution (particularly at P#1) results in a lower energy configuration compared with Li-site substitution, suggesting a thermodynamic driving force for Zr^{4+} to preferentially occupy P positions. However, when P#3 in $PS_4{}^{3-}$ is replaced, the ionic conductivity shows negligible improvement.

Although both Cl^- and Zr^{4+} doping independently enhance the ionic conductivity of $Li_7P_3S_{11}$, their effects are not additive due to distinct mechanisms of action. As shown in Fig. 4F, the maximum observed improvement in ionic conductivity is about 114% ($Li_{25}P_{11}ZrS_{40}Cl_4$#1). However, this enhancement is accompanied by increased structural instability compared to $Li_7P_3S_{11}$.

To further investigate the impact of dopants on the ion transport, the electrostatic potential (ESP) distributions on the electron density van der Waals surface were analyzed. As shown in Fig. 4G, the ESP around corner S is approximately −11.6 eV, while that around the bridge S (S4) is about −14.4 eV. When Cl replaces S2 to generate a $P_2S_6Cl^{3-}$ unit, not only does the ESP on the Cl-doped side drop to −8.5 eV, but the overall ESP also decreases. This would weaken the ionic bond between $P_2S_6Cl^{3-}$ and Li^+, which, combined with the increased free volume per Li^+ (Fig. 4D), ultimately enhances the ionic conductivity. By contrast, Zr-doped $P_2S_7{}^{4-}$ exhibits a lower ESP, resulting in a more stable structure. In particular, the gap in $PZrS_7{}^{5-}$ expands from 3.9 Å to 4.1 Å. Moreover, there is a structural transformation of $PZrS_7{}^{5-}$ during diffusion, where the length of S1–S5 is shortened from 4.1 Å at the beginning to 3.1 Å, facilitating the formation of new Zr–S bonds and creating novel Li^+ ion channels. This transformation is exclusive to Zr^{4+} doping into $P_2S_7{}^{4-}$, highlighting that the inclusion of Zr^{4+} makes $P_2S_7{}^{4-}$ more flexible and prone to fluctuations.[65,66]

3 Conclusions

In this work, a novel metal halide dopant, $ZrCl_4$, was introduced into the $Li_7P_3S_{11}$ solid electrolyte to simultaneously enhance its ionic conductivity, CCD, activation energy, and long-term stability with lithium metal anodes. The optimized dopant content (ESE-2) increased the ionic conductivity by 67% and CCD by 209%. DFT and AIMD simulation results revealed that Cl enhances ionic conductivity by introducing Li vacancies, while Zr increases ionic conductivity by improving dynamic structural flexibility. Also, Li/Li symmetrical cells with ESE showed significantly lower overpotential and extended cycling stability compared to those with control SE proving the potential of metal halide doping. Furthermore, a thin polymeric layer of SPE was employed as a catholyte in Li/LFP full cells. This configuration enabled stack pressure-free operation of ASSLBs, eliminating the need for time-consuming protective layer coating on cathode particles and complex, custom built cycling set ups generally used for cycling ASSLBs. The Li/LFP ASSLBs incorporating the ESE exhibited higher discharge capacity and improved capacity retention relative to the cells based on control $Li_7P_3S_{11}$ electrolyte.

Conflicts of interest

The authors declare no conflict of interest.

Author contributions

MBS: design of the project; experimental executions, data analyses, conceptualization, writing, reviewing; MBF: conceptualization, analyses, writing, reviewing; HL: analyses, writing, reviewing, conceptualization; HZ: DFT, AIMD, writing, reviewing; BK: XPS analyses, reviewing; SR: experimental executions, analyses, validation, reviewing; AB: writing, reviewing; XW: Raman spectroscopy, reviewing; YZ: writing, reviewing; RQ: reviewing, electrochemical performance analyses; IDH: Raman spectroscopy, reviewing; YW: DFT, AIMD, reviewing; JHH: XPS analyses, reviewing; ZF: experimental executions, analyses, validation, reviewing; QQ: conceptualization, data analyses, writing, reviewing.

Data availability

The data related to the current findings are included as the SI. Supplementary information is available. See DOI: **https://doi.org/10.1039/d5ta06438d**.

Acknowledgements

This work was financially supported by Syracuse University and NSF IUCRC Center for Solid-State Electric Power Storage (CEPS) grant number 2052611.

References

1 K. J. Kim, M. Balaish, M. Wadaguchi, L. Kong and J. L. Rupp, *Adv. Energy Mater.*, 2021, **11**, 2002689.

2 L. Wang, Z. Wu, J. Zou, P. Gao, X. Niu, H. Li and L. Chen, *Joule*, 2019, **3**, 2086–2102.

3 J. Ma, Y. Li, N. S. Grundish, J. B. Goodenough, Y. Chen, L. Guo, Z. Peng, X. Qi, F. Yang and L. Qie, *J. Phys. D: Appl. Phys.*, 2021, **54**, 183001.

4 R. Pathak, K. Chen, A. Gurung, K. M. Reza, B. Bahrami, F. Wu, A. Chaudhary, N. Ghimire, B. Zhou and W. H. Zhang, *Adv. Energy Mater.*, 2019, **9**, 1901486.

5 R. Pathak, K. Chen, A. Gurung, K. M. Reza, B. Bahrami, J. Pokharel, A. Baniya, W. He, F. Wu and Y. Zhou, *Nat. Commun.*, 2020, **11**, 93.

6 A. Baniya, M. B. Saud, H. Li, M. B. Faheem, Y. Zhang, A. Thapa, R. S. Bobba, P. I. Kaswekar and Q. Qiao, *Sustain. Energy Fuels*, 2024, **8**, 3574–3582.

7 S. Wang, J. Zhang, L. Zhang, X. Hu, X. Qin, X. Yan, Z. Wang, X. Lu, Y. Xin and F. Kang, *Nano Energy*, 2024, **131**, 110255.

8 X. Hu, Z. Zhang, X. Zhang, Y. Wang, X. Yang, X. Wang, M. Fayena-Greenstein, H. A. Yehezkel, S. Langford and D. Zhou, *Nat. Rev. Mater.*, 2024, **9**, 305–320.

9 F. Bahmani, C. Rodmyre, K. Ly, P. Mack and A. White Smirnova, *Batteries*, 2024, **10**, 21.

10 F. Bahmani and A. W. Smirnova, *J. Mater. Chem. A*, 2025, **13**, 18732–18742.

11 Q. Zhang, D. Cao, Y. Ma, A. Natan, P. Aurora and H. Zhu, *Adv. Mater.*, 2019, **31**, 1901131.

12 S. Risal, C. Wu, F. Wang, S. Risal, F. C. R. Hernandez, W. Zhu, Y. Yao and Z. Fan, *Carbon*, 2023, **213**, 118225.

13 H. Dai, C. Gallagher, S.-M. Bak, L. Gomes, K. Yang, R. Dong, S. Badhrinathan, Q. Zhao, Y. Du and G. P. Pandey, *Energy Storage Mater.*, 2025, 104123.

14 Y. Liu, Y. Xin, B. He, F. Zhang, C. Wang and H. Tian, *Adv. Mater.*, 2025, **37**, 2417353.

15 H. Li, M. B. Faheem, M. B. Saud, B. Khan, Y. Zhang, C. D. Rodmyre, R. Qiao, X. Wang, P. Hauck and V. Kee, *Batteries Supercaps*, 2025, 2500404.

16 H. Zhang, C. Li, M. Piszcz, E. Coya, T. Rojo, L. M. Rodriguez-Martinez, M. Armand and Z. Zhou, *Chem. Soc. Rev.*, 2017, **46**, 797–815.

17 A. Baniya, A. Gurung, J. Pokharel, K. Chen, R. Pathak, B. S. Lamsal, N. Ghimire, R. S. Bobba, S. I. Rahman and S. Mabrouk, *ACS Appl. Energy Mater.*, 2022, **5**, 648–657.

18 N. Kamaya, K. Homma, Y. Yamakawa, M. Hirayama, R. Kanno, M. Yonemura, T. Kamiyama, Y. Kato, S. Hama, K. Kawamoto and A. Mitsui, *Nat. Mater.*, 2011, **10**, 682–686.

19 B. He, F. Zhang, Y. Xin, C. Xu, X. Hu, X. Wu, Y. Yang and H. Tian, *Nat. Rev. Chem.*, 2023, **7**, 826–842.

20 A. Gurung, J. Pokharel, A. Baniya, R. Pathak, K. Chen, B. S. Lamsal, N. Ghimire, W.-H. Zhang, Y. Zhou and Q. Qiao, *Sustain. Energy Fuels*, 2019, **3**, 3279–3309.

21 F. Mizuno, A. Hayashi, K. Tadanaga and M. Tatsumisago, *Solid State Ionics*, 2006, **177**, 2721–2725.

22 A. R. Stamminger, B. Ziebarth, M. Mrovec, T. Hammerschmidt and R. Drautz, *Chem. Mater.*, 2019, **31**, 8673–8678.

23 N. Kamaya, K. Homma, Y. Yamakawa, M. Hirayama, R. Kanno, M. Yonemura, T. Kamiyama, Y. Kato, S. Hama and K. Kawamoto, *Nat. Mater.*, 2011, **10**, 682–686.

24 S. Chen, D. Xie, G. Liu, J. P. Mwizerwa, Q. Zhang, Y. Zhao, X. Xu and X. Yao, *Energy Storage Mater.*, 2018, **14**, 58–74.

25 H. Yamane, M. Shibata, Y. Shimane, T. Junke, Y. Seino, S. Adams, K. Minami, A. Hayashi and M. Tatsumisago, *Solid State Ionics*, 2007, **178**, 1163–1167.

26 Y. Onodera, K. Mori, T. Otomo, A. C. Hannon, S. Kohara, K. Itoh, M. Sugiyama and T. Fukunaga, *J. Phys. Soc. Jpn.*, 2010, **79**, 87–89.

27 H. Gamo, A. Nagai and A. Matsuda, *Sci. Rep.*, 2021, **11**, 21097.

28 Y. S. Choi, Y. Lee, H. Ahn, J. Jeong, K. Y. Chung, D. O. Scanlon and J. C. Lee, *Carbon Energy*, 2024, **6**, e564.

29 R. Maniwa, M. Calpa, N. C. Rosero-Navarro, A. Miura and K. Tadanaga, *J. Mater. Chem. A*, 2021, **9**, 400–405.

30 A. Mirtaleb and R. Wang, *Solid State Ionics*, 2025, **423**, 116844.

31 J. Wu, S. Liu, F. Han, X. Yao and C. Wang, *Adv. Mater.*, 2021, **33**, 2000751.

32 Z. Wang, Y. Jiang, J. Wu, Y. Jiang, W. Ma, Y. Shi, X. Liu, B. Zhao, Y. Xu and J. Zhang, *Nano Energy*, 2021, **84**, 105906.

33 Y. Zhen, W. Yang, Z. Qin, M. Ji, Y. Qie, J. Li, G. Ren, Q. Xue, Y. Chi and W. Xing, *Electrochim. Acta*, 2024, **503**, 144888.

34 P. Yu, N. Ahmad, C. Zeng, L. Lv, Q. Dong and W. Yang, *ACS Appl. Energy Mater.*, 2022, **5**, 13429–13438.

35 R. Song, R. Xu, Z. Wang, M. Yang, X. Yan, C. Yu and L. Zhang, *J. Alloys Compd.*, 2022, **921**, 166125.

36 N. H. H. Phuc, H. Gamo, K. Hikima, H. Muto and A. Matsuda, *Energy Fuels*, 2022, **36**, 4577–4584.

37 A. Mirtaleb and R. Wang, *J. Am. Ceram. Soc.*, 2024, **107**, 3800–3812.

38 Y. Zhen, W. Yang, Z. Qin, M. Ji, Y. Qie, J. Li, G. Ren, Q. Xue, Y. Chi, W. Xing and H. Geng, *Electrochim. Acta*, 2024, **503**, 144888.

39 F. Mizuno, A. Hayashi, K. Tadanaga and M. Tatsumisago, *Electrochem. Solid-State Lett.*, 2005, **8**, A603.

40 M. Tatsumisago, F. Mizuno, A. Hayashi and K. Tadanaga, *Adv. Mater.*, 2005, **17**, 918–921.

41 M. K. Tufail, N. Ahmad, L. Yang, L. Zhou, M. A. Naseer, R. Chen and W. Yang, *Chin. J. Chem. Eng.*, 2021, **39**, 16–36.

42 J. Zhou, P. Chen, W. Wang and X. Zhang, *Chem. Eng. J.*, 2022, **446**, 137041.

43 A. Hayashi, K. Minami, S. Ujiie and M. Tatsumisago, *J. Non-Cryst. Solids*, 2010, **356**, 2670–2673.

44 M. Park, W. D. Jung, S. Choi, K. Son, H.-G. Jung, B.-K. Kim, H.-W. Lee, J.-H. Lee, H. Kim and M. Park, *J. Korean Ceram. Soc.*, 2016, **53**, 568–573.

45 B. Zhao, J. Wu, Z. Wang, W. Ma, Y. Shi, Y. Jiang, J. Jiang, X. Liu, Y. Xu and J. Zhang, *Electrochim. Acta*, 2021, **390**, 138849.

46 N. Ahmad, L. Zhou, M. Faheem, M. K. Tufail, L. Yang, R. Chen, Y. Zhou and W. Yang, *ACS Appl. Mater. Interfaces*, 2020, **12**, 21548–21558.

47 Z. Wang, Y. Jiang, J. Wu, Y. Jiang, W. Ma, Y. Shi, X. Liu, B. Zhao, Y. Xu and J. Zhang, *Nano Energy*, 2021, **84**, 105906.

48 Y. Li, J. Li, J. Cheng, X. Xu, L. Chen and L. Ci, *Adv. Mater. Interfaces*, 2021, **8**, 2100368.

49 B. Shao, R. Das, Y. Huang, R. Deng, S. Seelman and F. Han, *J. Mater. Chem. A*, 2023, **11**, 17035–17044.

50 T. A. Tu, T. V. Toan, L. T. Anh, L. Van Thang and N. H. H. Phuc, *RSC Adv.*, 2024, **14**, 5764–5770.

51 N. Zhang, Z. Song, Q. Wan, Q. Shen and C. Lin, *Appl. Surf. Sci.*, 2002, **202**, 126–130.

52 S. Wenzel, D. A. Weber, T. Leichtweiss, M. R. Busche, J. Sann and J. Janek, *Solid State Ionics*, 2016, **286**, 24–33.

53 F. Han, A. S. Westover, J. Yue, X. Fan, F. Wang, M. Chi, D. N. Leonard, N. J. Dudney, H. Wang and C. Wang, *Nat. Energy*, 2019, **4**, 187–196.

54 Y. Seino, M. Nakagawa, M. Senga, H. Higuchi, K. Takada and T. Sasaki, *J. Mater. Chem. A*, 2015, **3**, 2756–2761.

55 M. R. Busche, D. A. Weber, Y. Schneider, C. Dietrich, S. Wenzel, T. Leichtweiss, D. Schröder, W. Zhang, H. Weigand and D. Walter, *Chem. Mater.*, 2016, **28**, 6152–6165.

56 J. Li, Y. Li, Y. Wang, X. Wang, P. Wang, L. Ci and Z. Liu, *Energy Storage Mater.*, 2024, 103962.

57 D. Cao, Q. Li, X. Sun, Y. Wang, X. Zhao, E. Cakmak, W. Liang, A. Anderson, S. Ozcan and H. Zhu, *Adv. Mater.*, 2021, **33**, 2105505.

58 B. Zhao, J. Wu, Z. Wang, W. Ma, Y. Shi, Y. Jiang, J. Jiang, X. Liu, Y. Xu and J. Zhang, *Electrochim. Acta*, 2021, **390**, 138849.

59 L. Liu, H. Wang, D. Ye, H. Zhao, J. Zhang and Y. Tang, *ACS Appl. Mater. Interfaces*, 2024, **16**, 31341–31347.

60 Y. Lu, C. Z. Zhao, H. Yuan, X. B. Cheng, J. Q. Huang and Q. Zhang, *Adv. Funct. Mater.*, 2021, **31**, 2009925.

61 Y. Zhou, C. Doerrer, J. Kasemchainan, P. G. Bruce, M. Pasta and L. J. Hardwick, *Batteries Supercaps*, 2020, **3**, 647–652.

62 Y. Zhang, X. Sun, D. Cao, G. Gao, Z. Yang, H. Zhu and Y. Wang, *Energy Storage Mater.*, 2021, **41**, 505–514.

63 E. Gil-González, L. Ye, Y. Wang, Z. Shadike, Z. Xu, E. Hu and X. Li, *Energy Storage Mater.*, 2022, **45**, 484–493.

64 J. Zhang, G. Zhu, H. Li, J. Ju, J. Gu, R. Xu, S. Jin, J. Zhou and B. Chen, *Nano Res.*, 2023, **16**, 3516–3523.

65 Y. Lee, Y.-H. Kim, J.-H. An and J.-C. Lee, *Acta Mater.*, 2022, **235**, 118106.

66 D. Chang, K. Oh, S. J. Kim and K. Kang, *Chem. Mater.*, 2018, **30**, 8764–8770.